

# Simulations of the Propagation of Multiple-FM Smoothing by Spectral Dispersion on OMEGA EP

## Introduction

Smoothing by spectral dispersion<sup>1</sup> (SSD) is a technique that, when coupled with the use of a distributed phase plate (DPP), smoothes on-target laser illumination. The principle is shown in Fig. 134.10. Frequency modulation (FM) at a frequency  $\omega_M$  is applied to the laser beam. After transiting a diffraction grating, the beam is angularly deflected at  $\omega_M$  as its instantaneous frequency varies. In the far field of the beam, where the target is positioned, the focal spot is laterally deflected. If the deflection is sufficiently greater than the far-field feature size of a DPP located before the focusing lens, significant smoothing is obtained on a time-averaged basis.

The selection of the appropriate  $\omega_M$ , grating dispersion  $d\theta/d\lambda$ , asymptotic smoothing time  $\tau_{\text{asympt}}$ , and DPP feature size is subject to an optimization that depends on the target hydrodynamics and the particular Legendre modes to be reduced.<sup>2</sup> For the work described here, three simultaneous modulation frequencies were optimum,<sup>3</sup> therefore the “multi-FM” nomenclature.

The actual implementation of SSD puts the modulator(s) and the grating in the front end of the laser where the apertures and energies are small, thereby avoiding optical-damage issues and the high cost of large specialty optics such as gratings. This requires, however, the propagation of dispersed FM beams through the amplifier and frequency-conversion sections of the laser. Conversion of this dispersed FM to amplitude modulation (AM) becomes a concern, particularly in the high-energy/high-intensity sections of the laser. There are numerous mechanisms for the conversion of FM to AM,<sup>4</sup> particularly in fiber components. The conversion of FM to AM inherent in free-space propagation is the mechanism of exclusive concern in this article.

## FM-to-AM Conversion from Free-Space Propagation

### 1. Geometrical-Optics Model

Undispersed FM beams, by definition, have no AM. This condition is readily seen by examining the Bessel-function expansion of a single-tone FM signal,<sup>5</sup>  $E(t)$ :

$$\begin{aligned} E(t) &= A \exp[i\omega_0 t + i\delta \sin(\omega_M t)] \\ &= A \sum_{n=-\infty}^{+\infty} J_n(\delta) \exp[i(\omega_0 + n\omega_M)t], \end{aligned} \quad (1)$$

where  $J_n$  is the  $n$ th-order Bessel function,  $\delta$  is the modulation depth,  $\omega_0$  is the optical frequency,  $\omega_M$  is the modulation (tone) frequency, and  $A$  is a constant. Taking the magnitude of Eq. (1) leads to  $|E(t)| = A$ . Note that this result depends critically on maintaining the phase relationship<sup>6</sup> of each sideband in the

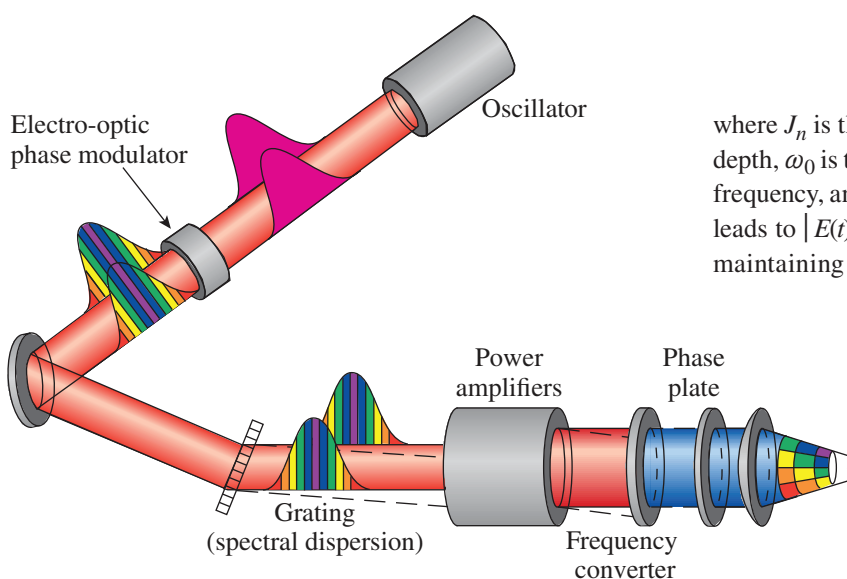


Figure 134.10 The smoothing by spectral dispersion (SSD) concept. Frequency modulation from one or more sequential electro-optic phase modulators is applied to the beam in the front end of the laser system prior to lateral magnification, amplification, and frequency conversion.

1723JR

Bessel-function expansion. This result may be readily extended to two-tone modulation:

$$\begin{aligned} E(t) &= A \exp\left[i\omega_0 t + i\delta_1 \sin(\omega_1 t) + i\delta_2 \sin(\omega_2 t)\right] \\ &= A \sum_{n=-\infty}^{+\infty} \sum_{m=-\infty}^{+\infty} J_n(\delta_1) J_m(\delta_2) \\ &\quad \times \exp\left[i(\omega_0 + n\omega_1 + m\omega_2)t\right] \end{aligned} \quad (2)$$

and so on for multitone modulation. The result is the same: as long as the sideband phases are maintained, there is no AM.

The effect of diffraction from the grating is to introduce a dephasing of the sidebands that depends on the sideband frequency, the dispersion of the grating, and the distance from the grating plane. Rewriting Eq. (1) with the grating dispersion in the  $y$  direction of a beam propagating in the  $z$  direction included yields

$$E(t) = A \sum_{n=-\infty}^{+\infty} J_n(\delta) \exp\left[i(\omega_0 + n\omega_M)t - i\mathbf{k}_n \cdot \mathbf{r}\right], \quad (3)$$

where  $\mathbf{k}_n \cdot \mathbf{r}$  is given by

$$\begin{aligned} \mathbf{k}_n \cdot \mathbf{r} &= \frac{\omega_0 + n\omega_M}{c} \left[ \sin(\theta_n) \mathbf{j} + \cos(\theta_n) \mathbf{k} \right] \cdot (y\mathbf{j} + z\mathbf{k}) \\ &= \frac{\omega_0 + n\omega_M}{c} \left[ y \sin(\theta_n) + z \cos(\theta_n) \right] \end{aligned} \quad (4)$$

with the  $z$  direction taken along the propagation direction of the fundamental frequency ( $n = 0$ ,  $z = 0$  at the grating),  $\mathbf{j}$  and  $\mathbf{k}$  being the unit vectors in the  $y$  and  $z$  directions, the  $\mathbf{r}$  vector being the distance from the grating to a point on the beam at coordinates  $(y, z)$ , and  $\theta_n$  being the propagation angle of the  $n$ th sideband. The angle  $\theta_n$  is given by

$$\theta_n = \frac{d\theta}{d\omega} n\omega_M. \quad (5)$$

Equation (3) demonstrates that for any finite distance from the grating, the sideband  $n$  becomes dephased from the pure-FM phasing by the quantity  $\mathbf{k}_n \cdot \mathbf{r}$ .

In the case of two-tone modulation, Eq. (3) becomes

$$\begin{aligned} E(t) &= A \sum_{n=-\infty}^{+\infty} \sum_{m=-\infty}^{+\infty} J_n(\delta_1) J_m(\delta_2) \\ &\quad \times \exp\left[i(\omega_0 + n\omega_1 + m\omega_2)t - \mathbf{k}_{n,m} \cdot \mathbf{r}\right], \end{aligned} \quad (6)$$

where  $\mathbf{k}_{n,m} \cdot \mathbf{r}$  is given by

$$\mathbf{k}_{n,m} \cdot \mathbf{r} = \frac{\omega_0 + n\omega_1 + m\omega_2}{c} \left[ y \sin(\theta_{n,m}) + z \cos(\theta_{n,m}) \right] \quad (7)$$

and  $\theta_{n,m}$  is given by

$$\theta_{n,m} = \frac{d\theta}{d\omega} (n\omega_1 + m\omega_2) \quad (8)$$

and so on for multitone modulation.

Because this dephasing is a function of  $\mathbf{r}$ , it leads to not only temporal AM but also spatial AM. Chuang<sup>7</sup> developed an analytic expression for the spatiotemporal AM from a single modulator in the geometrical-optics approximation. In the case of free-space propagation, the intensity  $I(y, z, t)$  in a plane at a distance  $z$  from the grating is given by<sup>7</sup>

$$I(y, z, t) = \frac{I_0}{\left\{ 1 + \frac{\delta\beta^2 z}{k_0} \sin\left[\omega_M t + \beta y_0(y, z, t)\right] \right\}}, \quad (9)$$

where  $I_0$  is the intensity at the grating plane (assumed to be at  $z = 0$ ) and  $y_0$  is the  $y$  location of the ray being traced at  $z = 0$ . Note that since the beam has not yet propagated any distance,  $I_0$  will have no SSD-induced time variation or  $y$ - (dispersion) direction variation. The quantity  $\beta$  is the grating-induced shear in radians per unit transverse length in the dispersion direction at the modulation frequency  $\omega_M$ . A straightforward calculation of the shear<sup>8</sup> yields

$$\beta = 2\pi \frac{d\theta}{d\lambda} \frac{\omega_M}{\omega_0}. \quad (10)$$

The result in Eq. (9) is valid where diffraction effects are negligible. Since some regions of  $I_0$  will have positive phase curvature (i.e., be focusing), there will exist a critical distance  $z_c$  at which the intensity goes to infinity (i.e., a caustic exists) in

the geometrical-optics approximation and Eq. (9) is no longer valid. This is trivially seen by inspecting the denominator in Eq. (9). At

$$z = z_r = \frac{k_0}{\delta\beta^2} \quad (11)$$

the denominator of Eq. (9) is equal to zero where the sine function is equal to  $-1$ . The distance  $z_r$  is termed the “critical distance.”

It is more physically intuitive to derive this result from a wavefront curvature standpoint. This is shown in Fig. 134.11. From Eq. (4) we may write the expression for the wavefront in terms of either the phase  $\phi$  or the optical path difference (OPD)  $z$  as:

$$\begin{aligned} \phi &= \delta \sin(\omega_M t + \beta y), \\ z &= \frac{\delta}{k_0} \sin(\omega_M t + \beta y). \end{aligned} \quad (12)$$

The critical distance  $z_r$  is calculated by applying the expression for the radius of curvature of an arc at the point  $\omega_M t + \beta y = -\pi/2$  where the wavefront is focusing:

$$z_r = \left. \frac{[1 + (dz/dy)^2]^{3/2}}{d^2 z / dy^2} \right|_{\omega_M t + \beta y = -\pi/2}. \quad (13)$$

Inserting the expression in Eq. (12) for the OPD  $z$  into Eq. (13) yields

$$\begin{aligned} z_r &= \frac{k_0 \left\{ 1 + \left[ \frac{\delta\beta}{k_0} \cos(\omega_M t + \beta y) \right]^2 \right\}^{3/2}}{-\delta\beta^2 \sin(\omega_M t + \beta y)} \bigg|_{\omega_M t + \beta y = -\pi/2} \\ &= \frac{k_0}{\delta\beta^2} \end{aligned} \quad (14)$$

for the critical distance. The critical distance  $z_r$  plays the same role as a focal length in geometrical optics. As such, the usual geometrical-optics formulae may be applied to it.

For distances  $z < z_r$ , the model in Eq. (9) can be used to visualize the spatiotemporal modulation related to the propagation of SSD. The case of a  $1.054\text{-}\mu\text{m}$ -wavelength,  $0.75\text{-ns} \times 10\text{-cm}$

FWHM (full width at half maximum) Gaussian pulse modulated at  $10\text{ GHz}$ ,  $\delta = 4\text{ rad}$  with  $60\text{-}\text{\AA}/\mu\text{rad}$  dispersion is shown in Fig. 134.12. Note that a similar plot of the intensity versus

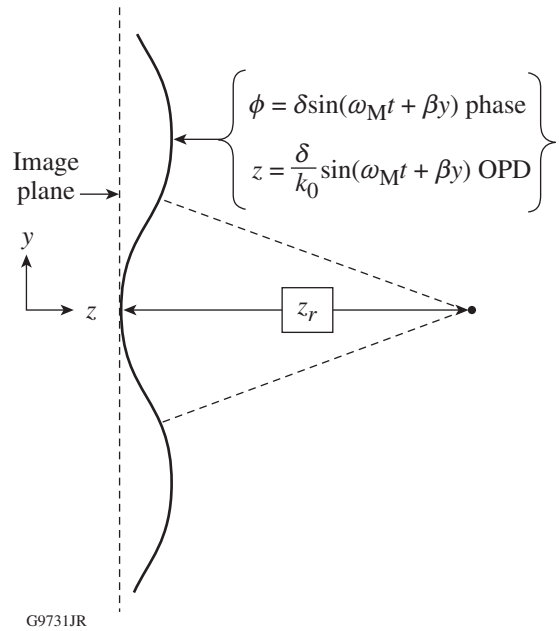


Figure 134.11 Schematic of the calculation of the critical distance  $z_r$ , from the local radius of curvature of the phase front. The usual formula for the curvature of an arc is applied to the expression for the optical path difference (OPD) at the location of positive phase curvature or  $\omega_M t + \beta y = -\pi/2$ .

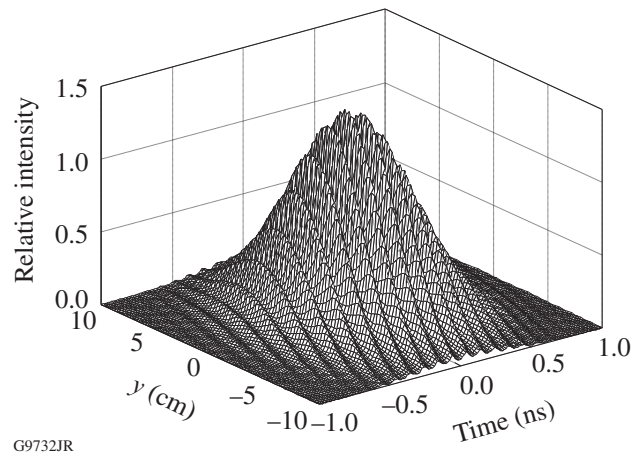


Figure 134.12 Relative intensity 2000 cm from the grating for a  $0.75\text{-ns} \times 10\text{-cm}$  FWHM Gaussian pulse phase modulated with  $\delta = 4\text{ rad}$  at  $10\text{ GHz}$  with  $60\text{-}\text{\AA}/\mu\text{rad}$  dispersion. This is a replot of Fig. 6-2 in Chuang’s thesis.<sup>7</sup>

$x, t$  rather than  $y, t$  would show no modulation. It is worth noting that for this particular example,  $z = 2000$  cm and  $z_r = 6800$  cm; therefore the geometrical-optics condition for validity is well satisfied. The ratio of  $z/z_r \sim 0.3$  is typical of the ranges of interest for large laser systems. Figure 134.13 displays lineouts in the temporal and spatial dispersion directions. The intensification relative to the unmodulated beam becomes of concern in those regions of a laser where the beam is close to the coating-damage, self-focusing, or stimulated-scattering limits.

From Eq. (9) an expression may be written for the normalized peak-to-valley amplitude modulation  $\alpha$ , assuming that the slowly varying envelope is removed:

$$\alpha(z) = \frac{I_{\max} - I_{\min}}{(I_{\max} + I_{\min})/2} = \frac{2\delta\beta^2 z}{k_0}. \quad (15)$$

From Eq. (15) it is seen that the normalized peak-to-valley modulation, in the geometrical-optics limit, is proportional to the propagation distance  $z$ , the modulation index  $\delta$ , and the square of the shear  $\beta$ .

## 2. Linear-Dispersive-Filter Model

Hocquet *et al.*<sup>9</sup> developed a similar metric termed a “distortion criterion” for temporal AM caused by SSD propagation away from a grating. Starting with the concept of free-space propagation as a linear dispersive filter,<sup>10</sup> the temporal Fourier transform of the electric field,  $E(z, \omega)$ , at a distance  $z$  from a grating is written as

$$E(z, \omega) = E_0(\omega) H(z, \omega), \quad (16)$$

where  $H(z, \omega)$  is a Fourier-domain transfer function. In the case of a grating, this transfer function is a phase-only filter. The phase can be expanded in a Taylor series in  $\omega$  of which the quadratic component  $\phi_2$ , the quadratic spectral phase, is the first term of interest for AM calculation. Assuming  $\phi_2$  is small, the transfer function is written as

$$H(z, \omega) = \left[ 1 - \frac{i}{2} \phi_2(z) \omega^2 \right]. \quad (17)$$

Substituting Eq. (17) into Eq. (16) and using Eq. (1) for  $E_0(\omega)$  and then inverse transforming and taking the magnitude of the resulting inverse transform yields

$$I(z, t) \approx 1 - \phi_2(z) \delta\omega_M^2 \cos(\omega_M t). \quad (18)$$

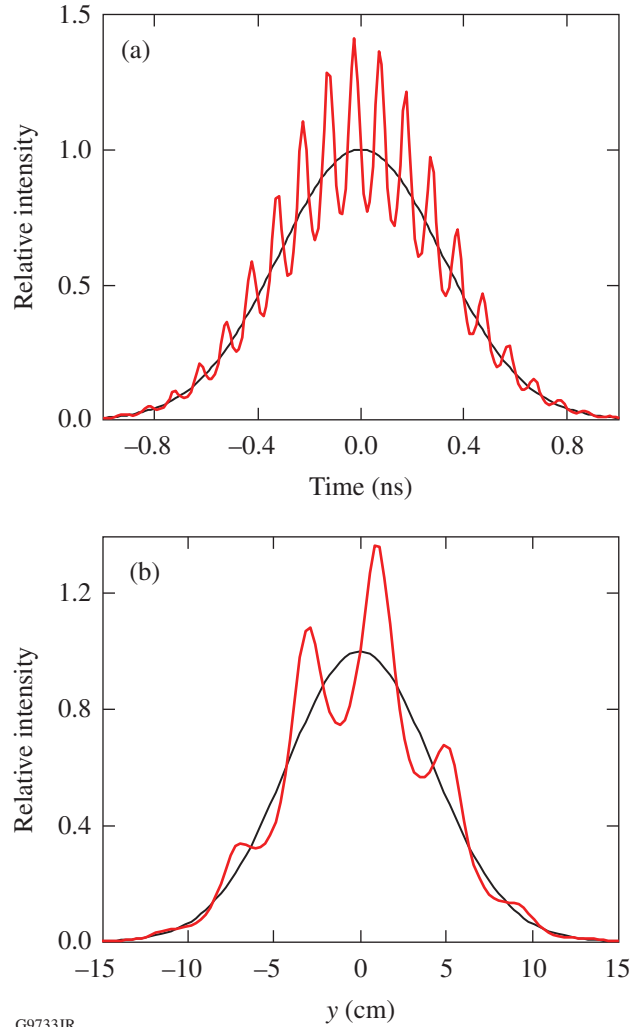


Figure 134.13

Lineouts (red line) in the temporal direction at  $(x, y) = (0, 0)$  and in the  $y$  (dispersion) direction at  $x = 0$  and  $t = 0$  of the relative intensity shown in Fig. 134.12. In both plots the unmodulated beam profile is also shown to illustrate the local intensification (black line).

Hocquet defines the “distortion criterion”  $\alpha$  as in Eq. (15). The values of  $I_{\max}$  and  $I_{\min}$  obtained by substituting  $\pm 1$  for the extrema of the cosine function in Eq. (18) lead to

$$\begin{aligned} \alpha(z) &= 2 \frac{1 + \phi_2(z) \delta\omega_M^2 - 1 + \phi_2(z) \delta\omega_M^2}{1 + \phi_2(z) \delta\omega_M^2 + 1 - \phi_2(z) \delta\omega_M^2} \\ &= 2\phi_2(z) \delta\omega_M^2. \end{aligned} \quad (19)$$

Substituting Chanteloup’s<sup>11</sup> expression for the quadratic part of the spectral phase  $\phi_2(z)$  at  $y = 0$ , the center of the beam, into Eq. (19) yields

$$\alpha(z) = \frac{2(2\pi)^2 c N^2}{\omega_0^3 \cos^2(\theta_0)} \delta\omega_M^2 z, \quad (20)$$

where a grating at Littrow angle  $\theta_0$  and a linear groove density of  $N$  per unit length have been assumed. Applying the expression for the dispersion of a grating at the Littrow angle

$$\left. \frac{d\theta}{d\lambda} \right|_{\theta=\theta_0} = \frac{N}{\cos(\theta_0)} \quad (21)$$

in Eq. (10) and substituting  $k_0 = \omega_0/c$ , Eq. (20) is seen to be identical to Eq. (15), which is Chuang's result.<sup>7</sup> The geometrical-optics and linear-dispersive-filter models, using completely different approaches, lead to the same result for the normalized peak-to-valley amplitude modulation. We choose to continue with Chuang's result since it provides a spatiotemporal description of the pulse intensification resulting from SSD propagation that may be readily compared to numerical models.

### 3. *B*-Integral Considerations

The so-called *B*- or "breakup" integral is an important measure of the transverse stability of a high-intensity beam. Physically, it is the integral of the local phase pushback in radians caused by propagation of the beam through media of thickness  $L$  with a positive  $\chi^3$ . By definition, it is

$$B \triangleq \frac{2\pi}{\lambda} \int_0^L \gamma I(x, y, z, t) dz, \quad (22)$$

where  $\gamma$  is a characteristic of the material.<sup>12</sup> In large laser systems, values of  $B$  in excess<sup>13</sup> of 2.0 to 2.2 rad between spatial filters can lead to catastrophic small-scale self-focusing of the beam. Laser-performance limits, particularly for temporally short pulses that do not experience significant gain saturation, are determined by the requirement to limit  $B$ . This is known as the "peak-power limit."

During laser design, the *B*-integral is calculated using the average local intensity; that is, transverse small-scale features that would be eliminated in a spatial-filtering operation are averaged out prior to computing  $B$ . In a system with SSD applied, the pinholes are carefully sized to ensure passage of the dispersed beam (at least to the Carson<sup>14</sup> limit =  $2\delta\omega_M$ ) through the system. The local intensification on any optical component induced by the propagation of SSD therefore needs to be carefully included in the calculation of the system's peak-power limit.

### Modeling

LLE's OMEGA EP laser is a multipass-architecture laser similar to that of the National Ignition Facility (NIF)<sup>15</sup> with important differences to optimize it for its primary mission of radiography of cryogenic implosions on the OMEGA laser<sup>16</sup> and separate flat-target experiments. The laser is shown schematically in Fig. 134.14. The multipass cavity formed by the end mirror and the deformable mirror is identical to that of the NIF. The input-output arm containing the booster amplifier is different, however, than that of the NIF. Because the beam-path distance to OMEGA EP's UV target chamber is significantly shorter than that to the NIF's (80 m versus ~140 m from the fold mirror to the target), the transport spatial filter is shorter. OMEGA EP's frequency-conversion crystals (FCC's) are located 8.1 m in front of the  $f/6.5$ , UV focus lens with a 3.4-m effective focal length. The most-damage-threatened component, the 4.0-cm-thick fused-silica vacuum window, is located 25 cm downstream of the focus lens in the converging beam. The distributed phase plate (DPP) is located 20 cm in front of the focus lens.

Unlike on the NIF, the 11-mm-/9-mm-thick, type-I/type-II, KDP/KD\*P frequency-conversion crystals are located on the floor upstream of the focus lens. The IR input polarization is vertical. The SSD dispersion direction is in the sensitive direction of the doubler (horizontal) at the FCC's.<sup>17</sup> The sign of the dispersion is chosen to compensate the frequency detuning<sup>18</sup> at the FCC's. A more-optimal choice, in terms of conversion efficiency, would have the dispersion direction in the sensitive direction of the tripler. The two UV transport mirrors immediately following the UV diagnostic beam splitter (DBS) are dichroic and strip residual  $1\omega$  and  $2\omega$  light from the beam so that only UV light is delivered to the focus lens.

Frequency conversion is an intensity-dependent nonlinear process that can increase amplitude modulation, particularly if operating in an unsaturated input intensity regime like the 11-mm-/9-mm-thick OMEGA EP FCC's. Since amplitude modulation from SSD propagation is minimized at the actual SSD grating and its image planes, the FCC's are located at a grating image plane. In the simulation, this is accomplished by translating the SSD grating in the front end of the system in the axial direction to make use of the large longitudinal magnification<sup>19</sup>  $M \sim 400$  ( $M = m^2$ , where  $m$  is the lateral magnification) of the system to shift the image. Magnification differs in the horizontal and vertical directions at least in part because of the large number of multipass tilted slabs.<sup>20</sup> Detailed ray-trace models of the system were used to set the SSD grating image on the FCC's.

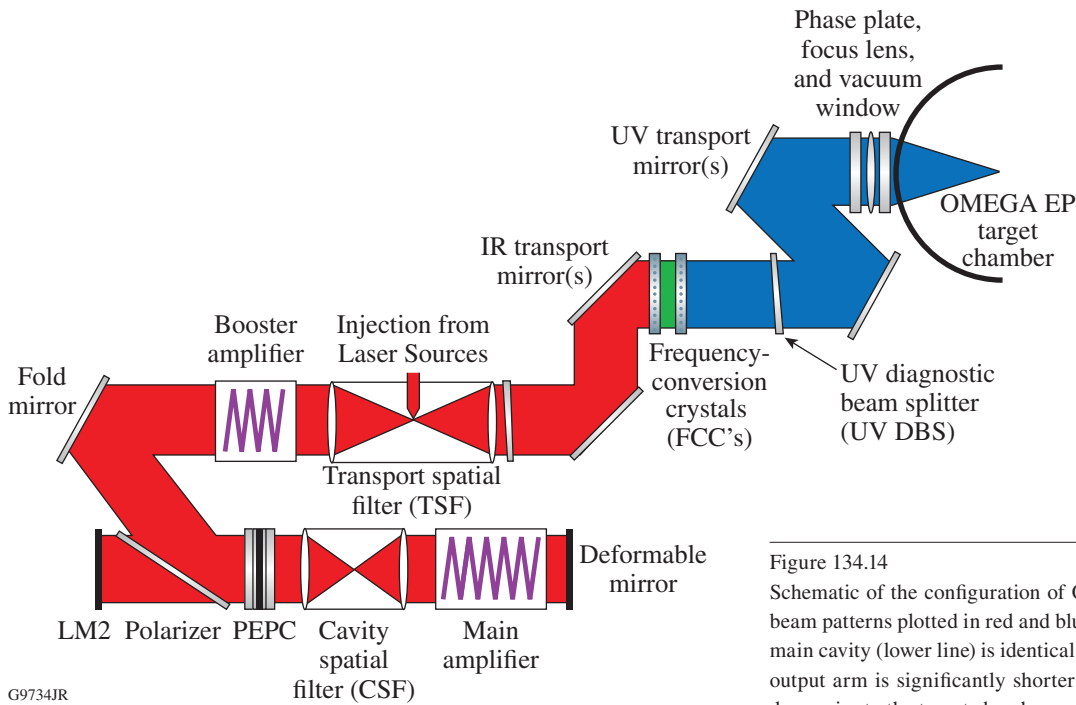


Figure 134.14  
Schematic of the configuration of OMEGA EP with IR and UV beam patterns plotted in red and blue respectively. The multipass main cavity (lower line) is identical to that of the NIF. The input-output arm is significantly shorter and frequency conversion is done prior to the target chamber.

The multi-FM temporal pulse shape consists of one to three “pickets” in front of a main compression “drive” pulse. A typical shape is shown in Fig. 134.15. Multi-FM SSD is applied to only one or more of the pickets; the system is capable of applying 17-GHz, single-FM SSD modulation to the drive pulse.<sup>21</sup> Although the available 17-GHz, single-FM SSD was not applied to the drive pulse for the majority of the demonstration shots,  $\delta = 5.5$  of 3.0-GHz stimulated Brillouin scattering suppression (SBSS) modulation was applied to the drive pulse for all the demonstration shots. The bulk of the on-target smoothing benefit is obtained prior to the second picket.<sup>2</sup> The pickets themselves have a UV FWHM of 150 ps.

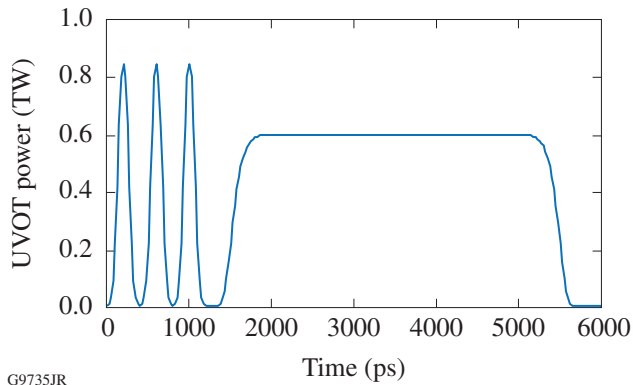


Figure 134.15  
Unsheared UV on-target (UVOT) pulse shape. The three pickets are followed by a main drive pulse.

The pickets shown in Fig. 134.15 are temporally short (150-ps FWHM in the UV, ~175 ps in the IR) compared to the main pulse. Because of their short pulse width, as these pickets increase in energy, they represent a peak-power threat to the system rather than an optical coating damage-fluence threat. It is therefore necessary to calculate the maximum *B*-integral attained at any spatiotemporal point in the pulse to assess the threat to the system. In order to do that for the complicated actual case of three modulators and laser system components including frequency conversion, the propagation code Miró is used.

Miró is a comprehensive laser design and simulation code developed<sup>22,23</sup> at CEA/CESTA, France. Miró models typical high-peak-power laser components and operations such as (but not limited to) free-space propagation, amplifiers, frequency converters, and gratings. Consistent with the progressively increasing levels of sophistication in the typical design process of high-peak-power lasers, Miró offers increasing levels of modeling sophistication in the form of “modes” of calculation starting with basic one-dimensional (1-D) ray tracing up to full diffraction calculation that includes broad-spectrum propagation with group-velocity dispersion.

For these simulations of multi-FM SSD, Miró’s “broad spectrum” mode and “inhomogeneous wave” grid transformation are used to render the problem computationally tractable. (For

more details, refer to the Miró V5<sub>ε</sub> Reference Manual.<sup>24</sup>) To ensure that the SSD model was being set up correctly in Miró, the analytical case of Chuang in Fig. 134.13, was first simulated. The results are shown in Fig. 134.16. The close agreement between the Miró prediction and the analytical treatment of Chuang gives confidence that the Miró SSD model has been constructed correctly and can be confidently used to predict AM in the region where  $z < z_r$ .

Since the expected picket energies are low (~100 J) and the beam areas are large (~1200 cm<sup>2</sup>), the picket fluence

(~0.08 J/cm<sup>2</sup>) is low compared to the equivalent (beam-normal) saturation fluence of the system (~5.7 J/cm<sup>2</sup>). The pickets are therefore in the small-signal-gain regime and their highest intensities are attained after the booster (final) amplifier, which has a small-signal gain of ~6. The highest *B*-integral, which is essentially an intensity/length product, is in the section of OMEGA EP downstream from the transport spatial filter to the target with the most-threatened component being the vacuum window on the target chamber. The relevant part of OMEGA EP is shown in Fig. 134.17.

The three modulation frequencies applied to the beam are detailed in Table 134.III. These modulation frequencies and their modulation depth have been chosen for optimal smoothing.<sup>25</sup> If the grating-induced beam shear across the nominal  $w = 35$ -cm beam width is given by

$$\Delta t = w \frac{2}{c} \tan(\theta), \tag{23}$$

where  $\theta$  is the angle of incidence on the grating (assumed to be at Littrow), then writing  $\tan(\theta)$  in terms of the dispersion  $d\theta/d\lambda$  yields

$$\Delta t = \frac{w\lambda}{c} \frac{d\theta}{d\lambda} = 360 \text{ ps} \tag{24}$$

for the temporal shear introduced by an 1800-lines/mm diffraction grating.

The phasing of the modulators in the Miró model is important to ensure that the *maximum* intensification is calculated. The 22.8- and 31.9-GHz modulators impart the most bandwidth to the beam and therefore the most local phase curvature. These modulators have a 9.1-GHz frequency difference, so near-maximum local wavefront curvatures can be expected in any pulse longer than ~110 ps. For this reason the modulators are modeled as *co*-sinusoidal modulators with zero relative phase and  $t = 0$  is centered on the picket.

Table 134.III: FM parameters for the multi-FM SSD system on OMEGA EP.

Modulator	1	2	3
Frequency (GHz)	21.165	22.838	31.881
IR modulation depth (radians)	0.450	1.040	2.071
IR bandwidth (Å)	0.7	1.8	4.9
IR dispersion (μrad/Å)	29.3	29.3	29.3
β (m <sup>-1</sup> )	136.9	147.7	206.3
z <sub>r</sub> (m)	707.9	263.1	67.8

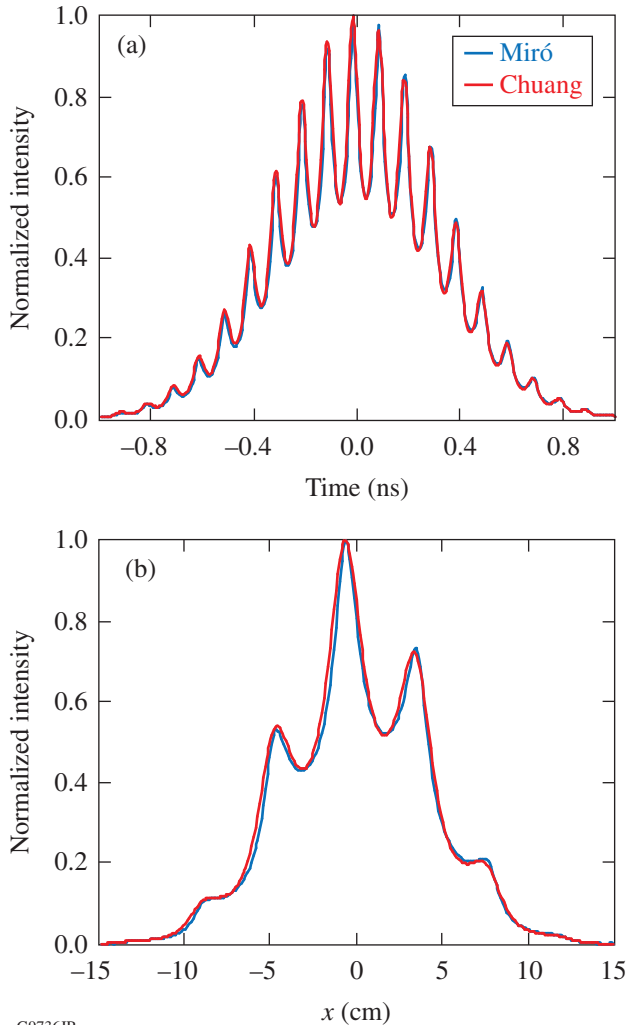


Figure 134.16 Lineouts of the relative intensity predicted by Miró (blue line) in the (a) temporal and (b) spatial directions for the case of Fig. 134.13 compared to the predictions of the Chuang model (red line) with  $\delta = 4$  rad at 10 GHz and 60-Å/μrad dispersion. This is at a distance from the grating of 2000 cm compared to  $z_r = 6800$  cm.

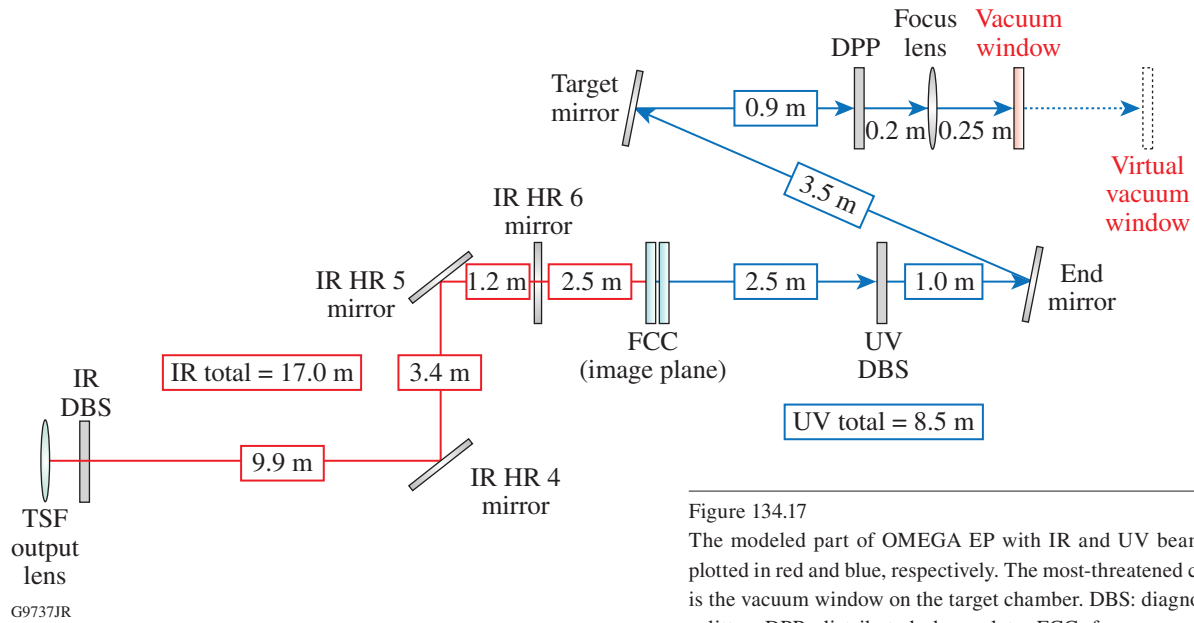


Figure 134.17

The modeled part of OMEGA EP with IR and UV beam patterns plotted in red and blue, respectively. The most-threatened component is the vacuum window on the target chamber. DBS: diagnostic beam splitter; DPP: distributed phase plate; FCC: frequency-conversion crystal; TSF: transport spatial filter; HR: high reflector.

To minimize amplification of AM in the frequency-conversion process, the SSD grating was carefully imaged onto the FCC's.<sup>26</sup> The component located the farthest from the image plane of the grating will experience the greatest intensification as a result of propagation. From Fig. 134.17 it is clearly seen that these components are the IR diagnostic beam splitter and the transport spatial filter's (TSF's) output lens upstream of the image plane and the vacuum window downstream of the image plane. The TSF output lens is  $\sim 17$  m from the image plane. When calculating the expected intensification, it is useful to first estimate how close the caustic is approached. To do that, the concept of critical distance  $z_r$  must be extended to a multifrequency-modulated beam. Recall from the discussion surrounding Fig. 134.11 that  $z_r$  is the radius of curvature of the wavefront caused by one modulation. At points in space and time where the frequency modulations are in phase, the resulting phase curvature is the sum of the individual phase curvatures. The thin-lens law<sup>27</sup> for two thin lenses in contact may be applied to add the phase curvatures where  $1/f$  is the power of a lens of focal length  $f$

$$\frac{1}{f_1} + \frac{1}{f_2} + \frac{1}{f_3} = \frac{1}{f_{\text{total}}} \quad (25)$$

to obtain

$$\frac{1}{z_{r,1}} + \frac{1}{z_{r,2}} + \frac{1}{z_{r,3}} = \frac{1}{z_{r,\text{total}}}, \quad (26)$$

where  $z_{r,i}$  is the critical distance corresponding to the  $i$ th modulation. Using Eq. (26) it is immediately found that  $z_{r,\text{total}}$  for this system is 50.1 m and the TSF output lens, 17 m from the image plane, is far from the caustic and in the region ( $z/z_r \sim 0.34$ ) where the Miró SSD model has been tested.

The vacuum window is in the UV section of OMEGA EP. The critical distance for the UV beam is required. Recall from Fig. 134.11 that

$$z_r = \frac{k_0}{\delta\beta^2} = \frac{k_{0,\text{IR}}}{\delta_{\text{IR}}\beta_{\text{IR}}^2} = \frac{k_{0,\text{UV}}/3}{(\delta_{\text{UV}}/3)\beta_{\text{UV}}^2} = \frac{k_{0,\text{UV}}}{\delta_{\text{UV}}\beta_{\text{UV}}^2} \quad (27)$$

because the propagation vector  $k_0$  triples after tripling to the UV ( $k_{0,\text{UV}} = 3k_{0,\text{IR}}$ ), the modulation index  $\delta$  is increased by a factor of 3 ( $\delta_{\text{UV}} = 3\delta_{\text{IR}}$ ), and the grating-induced shear in radians  $\beta$  at the modulation frequency is unchanged ( $\beta_{\text{UV}} = \beta_{\text{IR}}$ ). Equation (27) implies that for a single modulation,  $z_r$  is unchanged under frequency conversion. This is expected since the local wavefront radius of curvature is not expected to be changed by frequency conversion.<sup>28</sup> By Eq. (26) this also holds

for  $z_{total}$ . The vacuum window is located a physical distance of 8.5 m from the image plane and is therefore also far from the caustic and in the region where the Miró SSD model has been tested.

A screen shot of the Miró model used for these simulations is shown in Fig. 134.18 with the source shown in the lower left. The modeled beam was temporally 450 ps long and had an experimentally measured temporal profile. This is longer than the actual pickets propagated in the system and was chosen to ensure that multiple cycles of all three modulators were at the maximum intensity of the pulse shape. The spatial shape of the  $1\omega$  beam was a 20th-order, square super-Gaussian with 35-cm FWHM. The grid size for these simulations was  $16 \times 384 \times 1024 (x \times y \times u)$ , where  $y$  is the dispersion direction and  $u$  is the “inhomogeneous wave”<sup>29</sup> transformed grid coordinate.

The IR phase modulators and the reflection grating used in the model to disperse the beam are in the lower left. To reduce the model’s complexity and therefore computation time, the model’s phase modulation and SSD dispersion were applied at the 40-cm aperture (35-cm-sq beam). This required a model grating with 289.57 lines/mm used at its Littrow angle of  $8.78^\circ$  for  $\lambda = 1.054 \mu\text{m}$ . The distance in the model from the reflection grating to the cavity end mirror was adjusted to ensure the grating was imaged onto the mid-plane of the FCC’s.

Although the booster amplifier disks are included in the Miró model for future work, they are modeled as zero- $B$ -integral,

unity-gain optics to reduce computation time. The main laser cavity, including the cavity spatial filter (CSF), is modeled as a two-pass instead of the actual four-pass to model the imaging of the cavity while again reducing model computation time. All components in this early part of the laser have their nonlinear coefficient  $\gamma$  set to zero. All components from the TSF pinhole onward have their  $\gamma$ ’s specified to ensure  $B$  is accurately calculated. The  $\gamma$ ’s for the optical materials in OMEGA EP at their use wavelengths are detailed in Table 134.IV.

Three components have more than one wavelength on them simultaneously: the KDP doubler, the KD\*P tripler, and the fused-silica UV diagnostic beam splitter. The IR  $B$  contributed by the doubler consists of the  $B$  as a result of the IR beam itself and the cross-phase-modulation contribution caused by the  $2\omega$  beam on the IR beam. Similarly, its  $2\omega B$  contribution is the  $B$  attributed to the  $2\omega$  beam itself plus the cross-phase-modulation term contribution attributed to the IR beam. Where there are three wavelengths present as in both the tripler and the UV diagnostic beam splitter, the calculation is generalized for three waves. The actual calculation proceeds by finding the temporal maximum of the intensity and then calculating the  $B$  through the crystal by a split-step method.

The preceding calculates the *contribution* of the particular crystal to the  $B$ -integral. The  $B$ -integral at each harmonic does not start at a zero value and must be initialized.<sup>30</sup> For the doubler, the conservative assumption is made that the initially small divergence added to the fundamental frequency beam by nonlinear ripple growth ( $B$ ) is completely transferred to

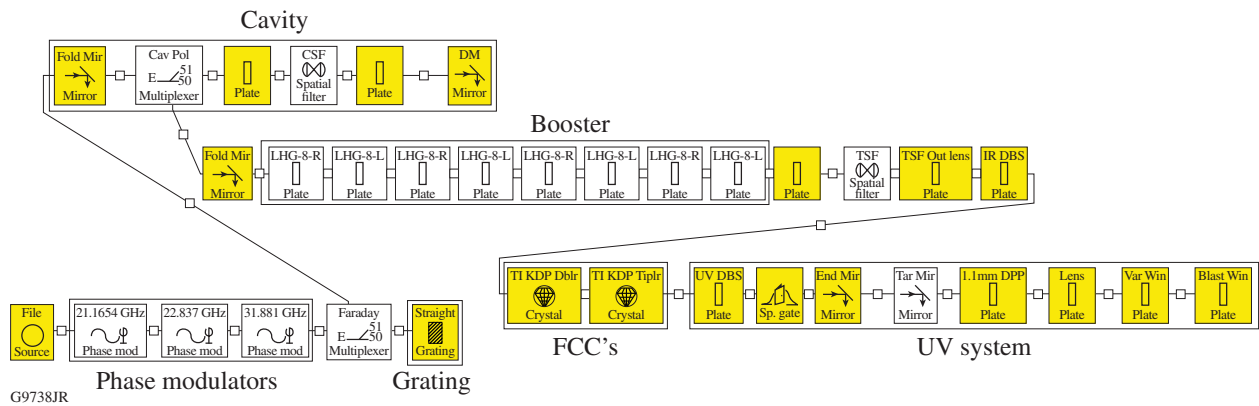


Figure 134.18 The OMEGA EP Miró model. The IR phase modulators are in the lower left. A reflection grating was used in the model to disperse the beam at the 40-cm aperture. Although the booster amplifier disks are included in this model, they are modeled as zero- $B$ -integral, unity-gain plates to reduce running time.

Table 134.IV: Nonlinear coefficients ( $\gamma$ ) for OMEGA EP components.

Component	Wavelength	Material	Thickness (cm)	$\gamma$ (cm <sup>2</sup> /GW)
TSF output lens	IR	fused silica	5.6	$2.7 \times 10^{-7}$
Diagnostic beam splitter	IR	fused silica	1.0	$2.7 \times 10^{-7}$
KDP doubler	IR and $2\omega$	KDP	1.1	$2.5 \times 10^{-7}$
KD*P tripler	IR, $2\omega$ , and UV	KD*P	0.9	$3.0 \times 10^{-7}$
Diagnostic beam splitter	IR, $2\omega$ , and UV	fused silica	1.0	$3.88 \times 10^{-7}$
Distributed phase plate	UV	fused silica	4.0	$3.88 \times 10^{-7}$
Focus lens	UV	fused silica	4.0	$4.00 \times 10^{-7(a)}$
Vacuum window	UV	fused silica	4.0	$4.86 \times 10^{-7(a)}$
Free space	IR or UV	air	various	$5.0 \times 10^{-10}$

<sup>(a)</sup>The component values have been increased to account for other effects.

the harmonic beam(s). By this assumption the initial  $B$  of the second harmonic ( $2\omega$ ) is simply set equal to the  $B$  of the fundamental beam.

The case of frequency tripling, which involves the mixing of two different frequencies, is more complicated. In this case Miró makes use of a phenomenological expression for the transmission  $T$  of a spatial filter<sup>31</sup> as a function of the  $B$ -integral  $B$ , and an experimentally determined “noise parameter”  $\varepsilon$ , for the system under consideration:<sup>32</sup>

$$T(B) = 1 - \frac{\varepsilon}{2} \left[ (1 + 2B^2) + \cosh(2B) \right]. \quad (28)$$

The loss  $L$  in transiting the spatial filter is from Eq. (27):

$$L(B) = \frac{\varepsilon}{2} \left[ (1 + 2B^2) + \cosh(2B) \right]. \quad (29)$$

Miró postulates that these losses, weighted by frequency (energy), are conserved in frequency conversion. This is roughly equivalent to postulating that the energy-weighted modulations on the beams to be mixed appear on the harmonic. Mathematically, the equation

$$\begin{aligned} & 3\omega \left[ 1 + 2B_{3\omega}^2 + \cosh(2B_{3\omega}) \right] \\ &= \sum_{n=1}^2 n\omega \left[ 1 + 2B_{n\omega}^2 + \cosh(2B_{n\omega}) \right] \end{aligned} \quad (30)$$

is solved numerically for  $B_{3\omega}$ , given  $B_{1\omega}$  and  $B_{2\omega}$ .

The focus lens is modeled as a 4-cm-thick plane-parallel plate of fused silica. The vacuum window is located 25 cm downstream of the 3.4-m effective-focal-length focusing lens in the converging beam. This portion of the UV system can be efficiently modeled by making use of the Talanov<sup>33</sup> transformation. To determine the beam modulation on the vacuum window, the beam is propagated the transformed distance  $z'$  with coordinates  $(x', y')$  given by

$$z' = \frac{z}{1 - z/f}, \quad (31)$$

$$(x', y') = \frac{(x, y)}{1 - z/f}. \quad (32)$$

This transformation yields the beam profile at the vacuum window by propagating the 40-cm aperture beam  $z' = 27$  cm instead of  $z = 25$  cm. Since only the resulting increase of the  $B$ -integral is of interest, rather than applying the transverse grid transformation in Eq. (32), the value of  $\gamma$  for the vacuum window was simply increased by the square of  $1/(1-z/f)$  to model the beam area's reduction and therefore intensity increase. This changed the value of  $\gamma$  from  $3.88 \times$  to  $4.52 \times 10^{-7}$  cm<sup>2</sup>/GW.

An additional complication of the model is the presence of the DPP 20 cm in front of the focusing lens. The DPP's spatial-phase modulation will itself be converted into spatial-amplitude modulation by propagation. The DPP's spatial phase will add and subtract from the SSD-induced phase in a complicated way. In the worst case, converging phase features from SSD and the DPP will increase the intensification. The DPP used for the OMEGA EP demonstration experi-

ments was designed at LLE<sup>34</sup> to produce a 1.1-mm-diam focal spot. Adequately resolving the phase features generated by this optic required very large spatial-grid resolutions ( $>1024 \times 1024$ ). Over the 47 cm of equivalent propagation distance from the DPP to the vacuum window, no caustics are generated. A simulation generated by propagating the design phase map of the DPP over the distances in question is shown in Fig. 134.19. In the absence of any other modulation, the peak intensity increase caused by modulation from the DPP on the focus lens and the vacuum window would be 3.2% and 7.6%, respectively. As a zero-order approximation to the effect of the DPP on  $B$ , the  $\gamma$ 's for the focus lens and the vacuum window were further increased by 3.2% and 7.6%, respectively, to  $4.00 \times 10^{-7} \text{ cm}^2/\text{GW}$  and  $4.86 \times 10^{-7} \text{ cm}^2/\text{GW}$ .

**Results**

The temporal shape used in the model is shown in Fig. 134.20, along with the modulators' waveform. This shape was taken from an early measurement of one of the IR pickets in the front end. The pickets generated for the OMEGA EP demonstration shot campaign were closer to Gaussian with a shorter (~150-ps) temporal width. The advantage of wider pickets for these simulations is to ensure that the peak temporal intensity extends over the time the modulators are co-phased. Since OMEGA EP operates in the small-signal regime for these pickets, it is an excellent representation of the picket at the TSF lens output.

The  $B$ -integral as a function of distance from the FCC's for the maximum power determined by a  $B$ -integral limit equals 2.0, as shown in Fig. 134.21. The UV  $B$ -integral starts at 0.5 rad

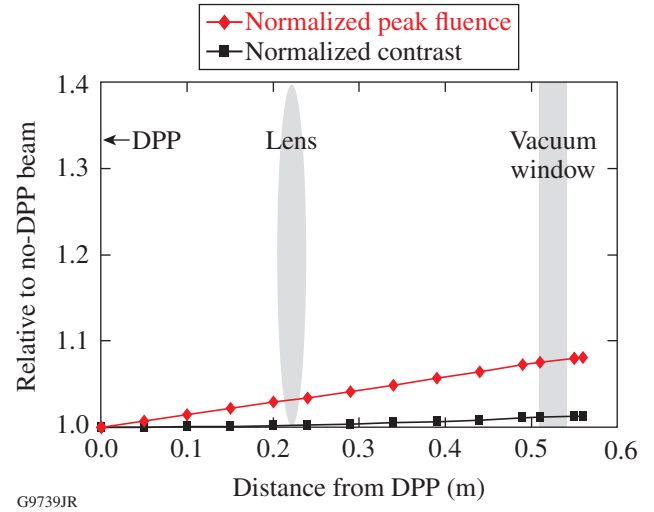


Figure 134.19  
The normalized peak fluence and the normalized contrast caused by modulation from the 1.1-mm-spot DPP as a function of distance from the DPP.

at the FCC's largely because of the IR contribution from the TSF output lens and the IR DBS. This result was obtained by adjusting the peak input intensity until a  $B$ -integral of 2.0 was obtained. This was achieved at a peak UV power measured at the vacuum window of 1.6 TW, which represents an upper bound for the picket power.

This result is the  $B$ -integral due only to AM resulting from the propagation of multi-FM SSD in the OMEGA EP Laser System. Many other effects have been neglected in this analysis including, but not limited to, gain narrowing in the amplifiers, etaloning in beamline components, etc. Therefore, this result is *not* the ultimate peak-power limit of OMEGA EP with multi-

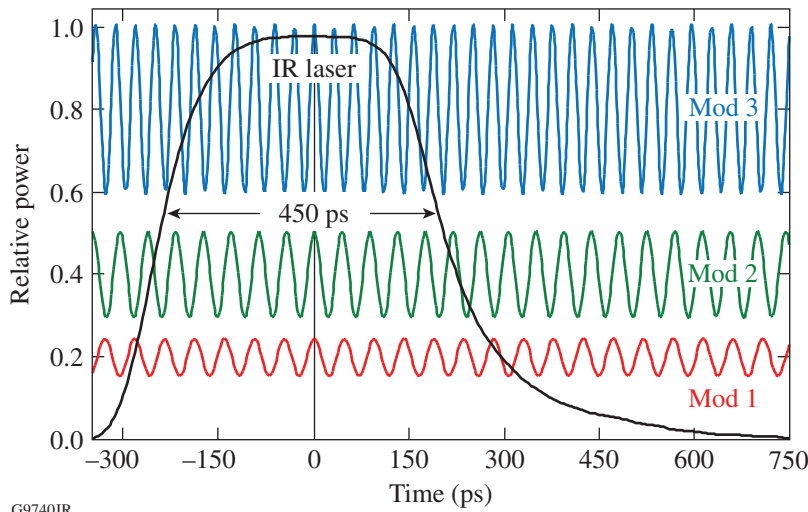
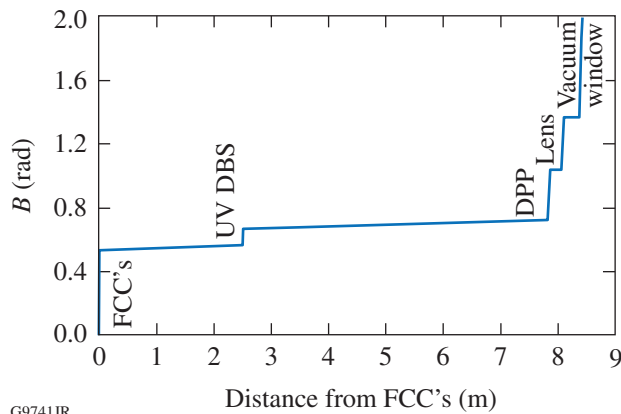


Figure 134.20  
The IR pulse shape used in the modeling along with the modulator waveforms.



G9741JR

Figure 134.21

$B$ -integral as a function of distance from the FCC's for a 710-J, 444-ps pulse of 1.60-TW peak power. The  $B$ -integral at the output of the vacuum window for this pulse is 2.0 rad.

FM SSD applied. Indeed, there is significant uncertainty in this calculation simply caused by the knowledge of the  $\gamma$ 's of each of the materials.

### Conclusions and Additional Work

An estimate of the peak-power limit resulting from the addition of multi-FM SSD to the OMEGA EP Laser System has been calculated. A connection was made between the work of Chuang<sup>7</sup> and the work of Hocquet,<sup>9</sup> and it was shown that their predictions are the same. The advanced laser design code Miró was then applied to first computationally replicate the results of Chuang and then compute the OMEGA EP peak-power limit in the presence of multi-FM SSD. This peak-power limit then becomes one part of a budget that determines the actual on-target peak-power limit of the system.

The  $B$ -integral is a convenient metric to rapidly estimate the damage threat to a system from self-focusing. The actual threat to the final optic is most accurately assessed<sup>35</sup> by comprehensive modeling that includes the phase contributions of all the system optics to directly model the beam filamentation at the vacuum window. Further work would involve high-resolution simulations to compute these effects. The issue of the longitudinal magnification should be addressed by an actual measurement on the system of the AM as a function of transverse beam location in the dispersion direction. Additional amplitude modulation caused by gain narrowing in the amplifiers can be added to the existing Miró model.

### ACKNOWLEDGMENT

This work was supported by the U.S. Department of Energy Office of Inertial Confinement Fusion under Cooperative Agreement No. DE-FC52-08NA28302, the University of Rochester, and the New York State Energy Research and Development Authority. The support of DOE does not constitute an endorsement by DOE of the views expressed in this article.

### REFERENCES

1. S. Skupsky, R. W. Short, T. Kessler, R. S. Craxton, S. Letzring, and J. M. Soures, *J. Appl. Phys.* **66**, 3456 (1989); in *LLE Review Quarterly Report* **78**, 62, Laboratory for Laser Energetics, University of Rochester, Rochester, NY, LLE Document No. DOE/SF/19460-295 (1999).
2. T. J. B. Collins, J. A. Marozas, K. S. Anderson, R. Betti, R. S. Craxton, J. A. Delettrez, V. N. Goncharov, D. R. Harding, F. J. Marshall, R. L. McCrory, D. D. Meyerhofer, P. W. McKenty, P. B. Radha, A. Shvydky, S. Skupsky, and J. D. Zuegel, *Phys. Plasmas* **19**, 056308 (2012).
3. J. A. Marozas, T. J. B. Collins, and J. D. Zuegel, "Multiple-FM Smoothing by Spectral Dispersion—An Augmented Laser Speckle Smoothing Scheme," to be submitted to the *Journal of the Optical Society of America B*.
4. J. E. Rothenberg, D. F. Browning, and R. B. Wilcox, in *Third International Conference on Solid State Lasers for Application to Inertial Confinement Fusion*, edited by W. H. Lowdermilk (SPIE, Bellingham, WA, 1999), Vol. 3492, pp. 51–61.
5. A. B. Carlson, *Communication Systems: An Introduction to Signals and Noise in Electrical Communication*, McGraw-Hill Electrical and Electronic Engineering Series (McGraw-Hill, New York, 1968), p. 228.
6. The correct phasing of the sidebands is such that all of the odd-order lower sidebands are  $\pi$  out of phase. For a very illustrative phasor representation of why this particular phasing eliminates AM and leads to pure frequency modulation, see Ref. 5, pp. 228–232.
7. Y.-H. Chuang, "Amplification of Broad-Bandwidth Phase-Modulated Laser Counterpropagating Light Waves in Homogeneous Plasma," Ph.D. thesis, University of Rochester, 1991.
8. Note that this result is independent of a grating being upstream from the modulator used to pre-shear the pulse.
9. S. Hocquet *et al.*, *Appl. Opt.* **47**, 3338 (2008).
10. J. W. Goodman, *Introduction to Fourier Optics* (McGraw-Hill, New York, 1968), p. 53.
11. J.-C. Chanteloup *et al.*, *J. Opt. Soc. Am. B* **17**, 151 (2000).
12. D. C. Brown, in *High-Peak-Power Nd:Glass Laser Systems*, edited by D. L. MacAdam, Springer Series in Optical Sciences (Springer-Verlag, Berlin, 1981), Vol. 25, Chap. 1, p. 45.
13. J. Trenholme, *Laser Program Annual Report 1974*, Lawrence Livermore National Laboratory, Livermore, CA, Report UCRL-50021-74, 197 (1975).

14. J. R. Carson, Proc. IRE **10**, 57 (1922).
15. C. A. Haynam *et al.*, Appl. Opt. **46**, 3276 (2007). In particular, see Fig. 4 in this reference.
16. Non-Major System Acquisition, NNSA Division of Secondaries and Inertial Fusion, NA-113.1, U.S. Department of Energy National Nuclear Security Administration, Washington, DC (1 May 2003).
17. The dispersion direction is horizontal in laser sources, is vertical in the main laser chain, and is horizontal again at the frequency-conversion crystals.
18. M. D. Skeldon, R. S. Craxton, T. J. Kessler, W. Seka, R. W. Short, S. Skupsky, and J. M. Soures, IEEE J. Quantum Electron. **28**, 1389 (1992).
19. R. S. Longhurst, *Geometrical and Physical Optics*, 3rd ed. (Longman, London, 1973).
20. R. Korniski and J. K. Lawson, in *International Optical Design Conference*, 2002 OSA Technical Digest Series (Optical Society of America, Washington, DC, 2002), Paper ITuD5.
21. It does, however, have a modest FM modulation to suppress stimulated Brillouin scattering in the UV optics.
22. O. Morice, Opt. Eng. **42**, 1530 (2003).
23. LLE makes use of Miró through the kind permission of CEA/CESTA.
24. Ph. Donnat *et al.*, MIRÓ V5<sub>e</sub> Reference Manual (1998).
25. J. A. Marozas, J. D. Zuegel, and T. J. B. Collins, Bull. Am. Phys. Soc. **55**, 294 (2010).
26. Since there are two FCC's, the grating was imaged to the midplane between them.
27. R. S. Longhurst, *Geometrical and Physical Optics*, 3rd ed. (Longman, London, 1973), p. 14.
28. This assumes, of course, that the normal to the wavefront remains within the tuning acceptance angle of the crystals.
29. O. Morice, X. Ribeyre, and V. Rivoire, in *Third International Conference on Solid State Lasers for Application to Inertial Confinement Fusion*, edited by W. H. Lowdermilk (SPIE, Bellingham, WA, 1999), Vol. 3492, pp. 832–838.
30. Ph. Donnat *et al.*, MIRÓ V5<sub>e</sub> Reference Manual (1998), Chap. 3, Sec. 3.12.6, pp. 162–164.
31. J. Trenholme *et al.*, *Shiva Nova CP&D Interim Report, Laser Fusion Program*, Lawrence Livermore National Laboratory, Misc. 107, 2-3-2-324 (1977); for a fuller discussion of this expression and its derivation, see D. C. Brown, in *High-Peak-Power Nd:Glass Laser Systems*, edited by D. L. MacAdam, Springer Series in Optical Sciences (Springer-Verlag, New York, 1981), Vol. 25, Chap. 7, Sec. 7.5, p. 216.
32. Here the fraction of noise power in the two frequency ranges of large ripples and fast-growing ripples has been assumed to be equal.
33. V. I. Talanov, JETP Lett. **11**, 199 (1970); for a discussion of the applicability of this transformation, see J. B. Trenholme and E. J. Goodwin, *Laser Program Annual Report 1976*, Lawrence Livermore National Laboratory, Livermore, CA, Report UCRL-50021-76, 2-339–2-344 (1976).
34. *Final Proposal for Renewal Award for Cooperative Agreement DE-FC52-92SF-19460* Between the U.S. Department of Energy and the Laboratory for Laser Energetics of the University of Rochester, Part I: Technical Program (Rochester, NY, 2007).
35. P. J. Wegner *et al.*, in *Optical Engineering at the Lawrence Livermore National Laboratory II: The National Ignition Facility*, edited by M. A. Lane and C. R. Wuest (SPIE, Bellingham, WA, 2004), Vol. 5341, pp. 180–189.